Impact of atmospheric CO 2 levels on continental silicate weathering

E. Beaulieu, Y. Goddéris, D. Labat, C. Roelandt, P. Oliva, B. Guerrero

Geochemistry Geophysics Geosystems G3

Article
Volume 11, Number 7
14 July 2010
Q07007, doi:10.1029/2010GC003078
ISSN: 1525-2027

Published by AGU and the Geochemical Society

Impact of atmospheric CO_2 levels on continental silicate weathering

E. Beaulieu, Y. Goddéris, and D. Labat
Laboratoire des Mécanismes et Transferts en Géologie, Université de Toulouse, Observatoire Midi-Pyrénées, CNRS, F-31400 Toulouse, France (beaulieu@lmtg.obs-mip.fr)

C. Roelandt
Geophysical Institute, University of Bergen, N-5007 Bergen, Norway

P. Oliva and B. Guerrero
Laboratoire des Mécanismes et Transferts en Géologie, Université de Toulouse, Observatoire Midi-Pyrénées, CNRS, F-31400 Toulouse, France

[1] Anthropogenic sources are widely accepted as the dominant cause for the increase in atmospheric CO_2 concentrations since the beginning of the industrial revolution. Here we use the B-WITCH model to quantify the impact of increased CO_2 concentrations on CO_2 consumption by weathering of continental surfaces. B-WITCH couples a dynamic biogeochemistry model (LPJ) and a process-based numerical model of continental weathering (WITCH). It allows simultaneous calculations of the different components of continental weathering fluxes, terrestrial vegetation dynamics, and carbon and water fluxes. The CO_2 consumption rates are estimated at four different atmospheric CO_2 concentrations, from 280 up to 1120 ppmv, for 22 sites characterized by silicate lithologies (basalt, granite, or sandstones). The sensitivity to atmospheric CO_2 variations is explored, while temperature and rainfall are held constant. First, we show that under 355 ppmv of atmospheric CO_2, B-WITCH is able to reproduce the global pattern of weathering rates as a function of annual runoff, mean annual temperature, or latitude for silicate lithologies. When atmospheric CO_2 increases, evapotranspiration generally decreases due to progressive stomatal closure, and the soil CO_2 pressure increases due to enhanced biospheric productivity. As a result, vertical drainage and soil acidity increase, promoting CO_2 consumption by mineral weathering. We calculate an increase of about 3% of the CO_2 consumption through silicate weathering (mol ha^{-1} yr^{-1}) for 100 ppmv rise in CO_2. Importantly, the sensitivity of the weathering system to the CO_2 rise is not uniform and heavily depends on the climatic, lithologic, pedologic, and biospheric settings.

Components: 10,300 words, 9 figures, 3 tables.

Keywords: CO_2; weathering; hydrology; evapotranspiration; vegetation.

Index Terms: 0414 Biogeosciences: Biogeochemical cycles, processes, and modeling (0412, 0793, 1615, 4805, 4912); 1009 Geochemistry: Geochemical modeling (3610, 8410); 1039 Geochemistry: Alteration and weathering processes (3617).

Received 10 February 2010; **Revised** 14 April 2010; **Accepted** 5 May 2010; **Published** 14 July 2010.

Beaulieu, E., Y. Goddéris, D. Labat, C. Roelandt, P. Oliva, and B. Guerrero (2010), Impact of atmospheric CO_2 levels on continental silicate weathering, *Geochem. Geophys. Geosyst.*, *11*, Q07007, doi:10.1029/2010GC003078.

1. Introduction

[2] Human activities are the dominant source for the CO_2 concentration increase in the atmosphere since the start of the industrial revolution, from 280 ppmv (part per million volume) in 1850 up to 387 ppmv in 2009. According to future anthropogenic emissions scenarios, this concentration may double before the end of the century [*Watson et al.*, 1990; *Friedlingstein et al.*, 2006; *Intergovernmental Panel on Climate Change*, 2007].

[3] Predicting how atmospheric CO_2 pressure will evolve in the future requires a quantitative description of the global carbon cycle. During the last decade, many processes have been explored and quantified, but continental weathering has thus far been neglected in most studies. Continental weathering of silicate rocks (granites, basalts) can be summarized by the following reaction describing the dissolution of a plagioclase mineral constitutive of a bedrock with coeval precipitation of kaolinite and production of dissolved species carried to the ocean by rivers:

$$4Na_{0.5}Ca_{0.5}Al_{1.5}Si_{2.5}O_8 + 17H_2O + 6CO_2(aq) \rightarrow 3Al_2Si_2O_5(OH)_4 + 2Na^+ + 2Ca^{2+} + 6HCO_3^- + 4H_4SiO_4(aq) \quad (1)$$

For each equivalent of alkalinity produced by reaction 1, one mole of atmospheric CO_2 has been consumed and transferred to the continental waters as bicarbonate ions. This atmospheric CO_2 consuming process, known as a first-order component of the geological carbon cycle (and hence of the long-term climate evolution of the Earth) [*Walker et al.*, 1981; *Donnadieu et al.*, 2006], seems to be also sensitive to the ongoing anthropogenic perturbation of the Earth system, as illustrated by two recent findings. Atmospheric CO_2 consumption through weathering in the Mississippi watershed has increased by 40% over the last 40 years [*Raymond et al.*, 2008]. Rapidly increasing weathering rates have been reported in Iceland [*Gislason et al.*, 2009] possibly in response to climate warming at high latitudes.

[4] Weathering is a complex process driven by many forcing functions, including climate, CO_2, land use, hydrology, physical erosion and vegetation cover, all these factors being tightly intertwined [*Gaillardet et al.*, 1999; *Millot et al.*, 2002; *Dessert et al.*, 2003; *Goddéris et al.*, 2009; *Roelandt et al.*, 2010]. Because of this complexity, the modeling method might be a way to unravel the processes at play in the suspected increase in continental weathering at the decadal scale, exploring the potential role of each parameter.

[5] In a recent modeling study, *Roelandt et al.* [2010] and *Goddéris et al.* [2009] have emphasized the key role played by land plants in weathering processes through the control they exert on the soil hydrology. As evapotranspiration is suspected to respond both to climate change and atmospheric CO_2 rise through biome and stomatal conductance changes [*Gerten et al.*, 2004], the question whether continental weathering is sensitive to these modifications is worth testing.

[6] In this study, we explore the weathering system sensitivity to the atmospheric CO_2 level for a variety of sites (22) all around the world (Figure 1), under specific climatologies and characterized by specific lithologies. In this first study, we deliberately limit the number of tested parameter to the atmospheric CO_2 level without accounting for the concomitant climatic change. Temperature and rainfall are thus held constant in the simulations. We use a coupled dynamic model: B-WITCH [*Roelandt et al.*, 2010], for continental vegetation and chemical weathering in soils and saprolite. This model is used to quantify the sensitivity of CO_2 consumption by silicate rock weathering at various atmospheric CO_2 levels from 280 to 1120 ppmv, accounting for the modification in soil hydrology linked to the biome response. Since the strength of the feedback existing between the solid Earth CO_2 degassing and CO_2 consumption through continental weathering [*Walker et al.*, 1981] depends on the efficiency of the response of silicate weathering to atmospheric CO_2 levels [*Berner*, 2004], such a quantification also constrains our understanding of the geological evolution of the global carbon cycle and climate.

2. Land Plants and CO_2 Levels

[7] The exchange between land plants and the atmosphere mainly consists of atmospheric CO_2 uptake through photosynthesis and water vapor release through the transpiration process [*Bonan*, 2002; *Hetherington and Woodward*, 2003]. The consequences of the atmospheric CO_2 increase on the global water balance and carbon cycle will at least partly depend on the biospheric response in term of stomatal conductance, photosynthesis, biome redistribution and evapotranspiration.

[8] Previous studies based on modeling or experimental methods showed that under high CO_2 con-

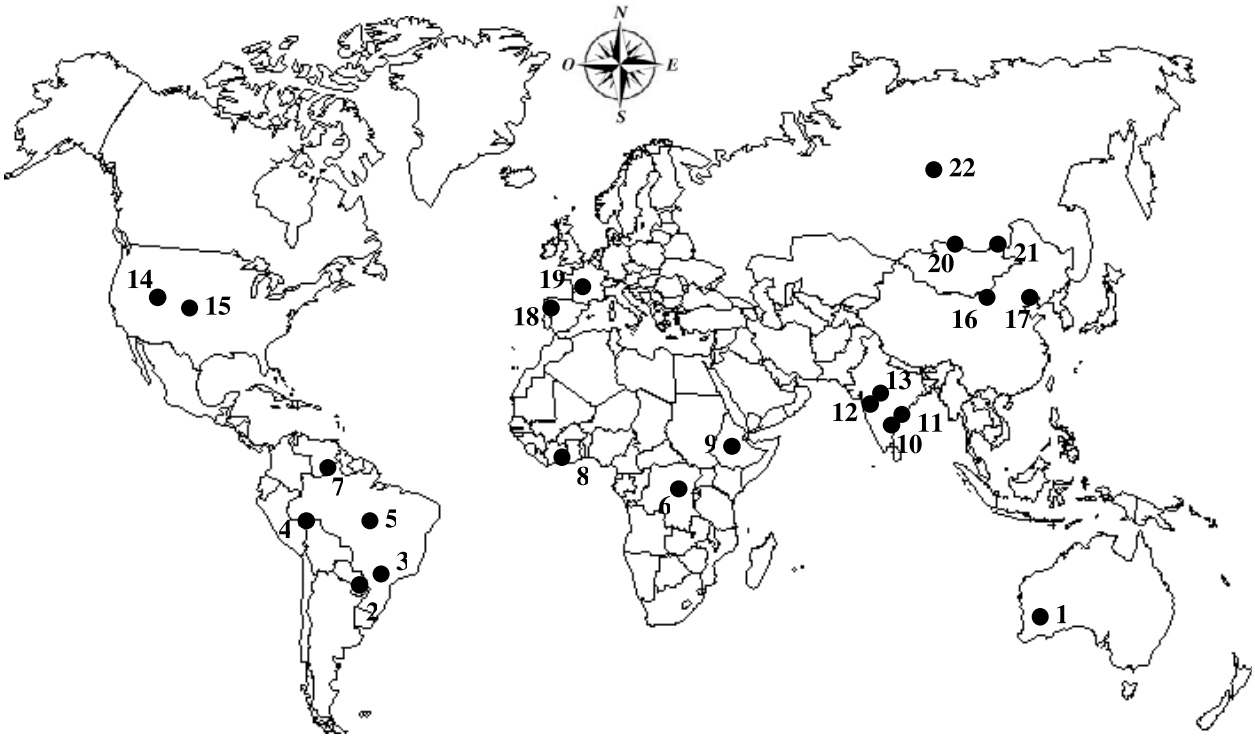

Figure 1. Localization of 22 grid cells on global map.

centrations, plants tend to close their stomata in order to reduce their transpiration, leading to an increase in the intercellular CO_2 pressure and finally a more efficient use of soil moisture [*Friend and Cox*, 1995; *Van de Geijn and Goudriaan*, 1997; *Hui et al.*, 2001; *Woodward*, 2002]. The precise quantification of the influence of the atmospheric CO_2 concentration increase on biospheric processes remains a matter of debate. Under a doubled CO_2 concentration, transpiration is predicted to decrease between 6% [*Leipprand and Gerten*, 2006] and 25% [*Friend and Cox*, 1995]. Calculated mean global evapotranspiration decreases by 7% while runoff and soil moisture increase by 5% and 1%, respectively [*Leipprand and Gerten*, 2006]. Finally, stomatal conductance displays a decrease ranging from 25% [*Field et al.*, 1995] up to 40% [*Morison and Gifford*, 1983] in experiments.

[9] With increasing atmospheric CO_2, any decrease in the evapotranspiration at constant rainfall will increase the drainage of the soils and saprolite, and will therefore impact the weathering rates. Any increase in the drainage may potentially decrease the residence time of the waters in contact with the minerals, thus inhibiting dissolution. However, as the net water flux exported from the soil and the saprolite increases, the net dissolved element export from the soil and saprolite may still potentially increase. Furthermore, any change in the residence time of water in the soil and saprolite may change the saturation state of the solutions with respect to the mineral phase, impacting on the weathering rates. Dissolution reactions are thus complex and generally highly nonlinear with respect to environmental factors such as the drainage. This is why we use a mechanistic model describing the dissolution reaction based on laboratory kinetic laws, while the water fluxes are estimated from the LPJ model simulations as detailed in section 3.

3. Model Description

[10] In this section, the coupling procedure between WITCH and LPJ models called B-WITCH is first described, followed by a brief description of the LPJ and WITCH models.

3.1. B-WITCH Model

[11] The basic principle of the B-WITCH model is the use of a global dynamic vegetation model to estimate the water balance in the weathering profiles (namely the vertical drainage and the water volumetric content of each soil layer). These hydrologi-

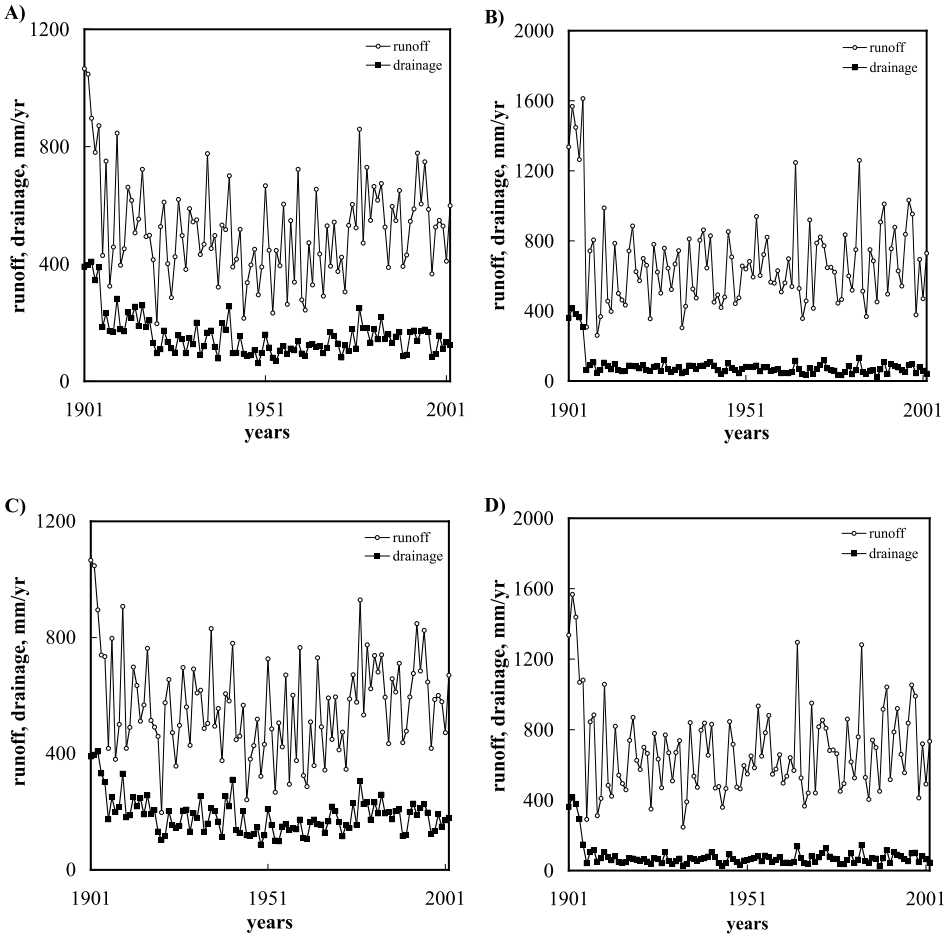

Figure 2. Drainage and surficial runoff in mm/yr calculated by LPJ model for a grid cell located in France (grid cell 19) for atmospheric CO_2 concentrations of (a) 355 ppmv and (b) 1120 ppmv and for a grid cell located in South America (grid cell 3) for atmospheric CO_2 concentrations of (c) 355 ppmv and (d) 1120 ppmv over the 1901–2002 period.

cal parameters are then transferred to a process-based model where the dissolution/precipitation rates of minerals in the weathering profile are calculated. The weathering profile is divided into three layers: one superficial soil layer (L1: from 0 to 0.5 m depth), one medium soil layer (L2: from 0.5 to 1.5 m depth) and one deep saprolitic layer (L3: from 1.5 to 6.5 m depth, 5 m thick) [*Roelandt et al.*, 2010]. The mineralogical composition of each layer is detailed in section 4. The thickness of the two upper layers is fixed by the geometry of the LPJ model.

[12] The LPJ model uses monthly mean climate information over the 1901–2002 period [*New et al.*, 2000; *Mitchell and Jones*, 2005] to estimate the atmosphere-vegetation-soil water exchanges and establish and stabilize the potential vegetation cover. At the end of the simulation, the soil hydrology is very close to steady state for all the investigated grid elements (Figures 2a and 2b). Then WITCH uses the mean annual surface runoff, drainage and volumetric water contents calculated by LPJ and mean climatic data over the last twenty years of 1901–2002 period. The model is run until steady state is reached (20 simulated years), i.e., when the chemical composition of the soil solutions has reached steady state. The CO_2 pressure in all layers of the soil and saprolite is calculated as a function of the below ground productivity *Pr* estimated by LPJ in g CO_2 m^{-2} yr^{-1} (litter and soil organic matter decomposition). The CO_2 pressure P_{max} (atm) below the root zone (saprolite layer) is calculated according to *Van Bavel* [1952]:

$$P_{\max} = P_{atm} + k_{unit}\frac{Pr \cdot L^2}{2 \cdot \phi \cdot D_s} \quad (2)$$

where L is the root zone depth (1.5 m), ϕ is the soil porosity (m^3 m^{-3}) and D_s is the CO_2 diffusivity. k_{unit} is a unit conversion factor (fixed at 1.957×10^{-3} m^2

atm g^{-1} CO_2). D_s (m^2 s^{-1}) is a function of air temperature T (in Kelvin), soil porosity (ISRIC database, see below), and tortuosity τ (fixed at 0.45) [*Gwiazda and Broecker*, 1994]:

$$D_s = 0.139 \cdot 10^{-4} \cdot \left(\frac{T}{273.15}\right)^2 \cdot \phi \cdot \tau \quad (3)$$

0.139×10^{-4} m^2 s^{-1} is the CO_2 diffusion coefficient of CO_2 in air at 273.15 K.

[13] At this stage, the B-WITCH model does not track the dynamics of the atmospheric CO_2 rise. As mentioned above, a set of 4 simulations is performed, with several constant atmospheric CO_2 levels (280, 355, 560, and 1120 ppmv), but always with the same climatic input. This procedure allows us to isolate the effect of atmospheric CO_2 on the vegetation and weathering dynamics. The coupling between the WITCH and the LPJ model is fully described by *Goddéris et al.* [2009] and *Roelandt et al.* [2010].

3.2. Weathering Model WITCH

[14] The numerical model simulating the chemical weathering reactions in the soil horizons (WITCH) is a box model that integrates the dissolution/precipitation rates of mineral phases and the chemical composition of the soil solution as a function of time. The time evolution of the soil solution chemistry is calculated at each time step solving the following equation:

$$\frac{d(z \cdot \theta \cdot C_j)}{dt} = F_{top} - F_{bot} + \sum_{i=1}^{n_m} F^i_{weath,j} - \sum_{i=1}^{n_m} F^i_{prec,j} \pm R_j \quad (4)$$

where C_j is the concentration of the species j. WITCH includes a budget equation for Ca^{2+}, Mg^{2+}, K^+, Na^+, SO_4^{2-}, total alkalinity, total aluminum, total silica, and total phosphorus. z is the thickness of the considered layer, and θ the water volumetric content (m^3 of water m^{-3} of soil). F_{top} is the input of species from the layer above the considered layer in moles s^{-1} m^{-2} through drainage, and F_{bot} is the removal through downward drainage. Both the drainage and the water volumetric content are taken from the biospheric model has explained below. R_j stands for the cation exchange flux between the soil solution and the clay-humic complex. This cation exchange flux is set to zero when a pluriannual steady state is calculated to save computation time. However, it is fully accounted for in a dynamic mode for seasonal simulations through the computation of a Fick diffusion law [*Goddéris et al.*, 2006].

[15] $F^i_{weath,j}$ is the release of the species j through dissolution of the mineral i in the considered box, and $F^i_{prec,j}$ is the removal through precipitation when saturation is reached (see below). n_m is the total number of mineral considered in the simulation. Those dissolution/precipitation terms are calculated for silicate minerals through laboratory kinetic laws derived from the transition state theory (TST) concept [*Eyring*, 1935] and rates are normalized to the BET surface. The overall dissolution rate F_g of mineral g inside a given layer is the sum of four parallel elementary reactions promoted by H^+, OH^-, water and organic ligands. Chemical speciation of the soil solution is calculated for 17 chemical species. A detailed description of the WITCH model is given by *Goddéris et al.* [2006, 2009], *Le Hir et al.* [2009], and *Roelandt et al.* [2010].

3.3. Global Dynamic Vegetation Model LPJ

[16] The Lund-Potsdam-Jena Dynamic Global Vegetation Model (LPJ) is derived from the BIOME family of models, and is able to represent terrestrial vegetation dynamics, carbon and water exchanges between land and atmosphere at the global scale. It combines fast processes such as feedback through canopy conductance between photosynthesis and transpiration, and slow processes such as resource competition, tissue turnover and population dynamics. In this model, 10 plants functional types (PFT) are differentiated by physiological, morphological, and phenological attributes. Each PFT is assigned bioclimatic limits (minimum coldest-month temperature for survival or maximum coldest-month temperature for establishment for example), which determine whether it can survive and/or regenerate under the climatic conditions prevailing in a particular grid cell. Photosynthesis, evapotranspiration and soil water dynamics are modeled on a daily time step, while vegetation structure and PFT population densities are updated annually. The LPJ model is fully described by *Sitch et al.* [2003].

4. Study Sites

4.1. Description

[17] Twenty-two grid cells (0.5°longitude × 0.5° latitude) were selected to cover a wide range of climatic and lithologic conditions. The simulations have been limited to a discrete number of grid cells because a precise knowledge of the mineralogical composition of the soil layers and of the underlying bedrock is absolutely necessary. No estimation of the weathering rates could be performed accurately

without this critical information. Although the lithological information can be gathered globally [*Hartmann et al.*, 2009], the soil mineralogy is difficult to define on a global scale. As demonstrated in several recent modeling studies [*Goddéris et al.*, 2006; *Maher et al.*, 2009], this mineralogical composition must be precisely defined: the draining waters first encounter the soil layers before reaching the saprolite, and their chemical composition might heavily imprinted by the dissolution reactions within the surficial soil layers. Gathering this soil mineralogical information is not easy because of the lack of data and of spatial heterogeneity.

[18] Three main type of silicate outcrops, i.e., basalt, granite, and sand/sandstones [*Amiotte-Suchet et al.*, 2003], are used to define the mineralogical composition of the deep saprolitic layer. The outcrops define a broad spectrum of weatherabilities and play a particular role in the long-term atmospheric CO_2 balance. Indeed, although they only account for 6% of the continental surface, the basalts play a major role in the carbon cycle and are among the more easily weathered silicate rocks [*Meybeck*, 1986; *Amiotte-Suchet and Probst*, 1993; *Millot et al.*, 2002; *Dessert et al.*, 2003]. The granites are less weatherable but also influence the long-term atmospheric CO_2 balance [*Gaillardet et al.*, 1999; *Millot et al.*, 2002; *Oliva et al.*, 2003]. Finally, the sands and sandstones are poorly weatherable owing to the nature of the dominant mineral (quartz). Although potentially important in the global carbon cycle [*Calmels et al.*, 2007], shale lithologies are not explored in this contribution because of large and almost unconstrainable variability in their clay composition.

[19] The 22 grid cells have been chosen to span a large range of climates (Figure 1). Nine grid cells are located in Asia (India; Russia; China), five in South America (Paraguay; Brazil; Venezuela), two in North America (USA), three in Africa (Ethiopia; Ivory Coast; DR Congo), two in Europe (Spain and France) and one in Australia. For a same bedrock type, the corresponding grid cells are located under different climates. Eight basaltic grid cells are characterized by oceanic (1), savanna (1), subarctic (1), semiarid (3) or humid subtropical (2) climates according to the chart of *Köppen* [1923]. Then, eight grid cells with a granitic bedrock are located under tropical (2), oceanic (1), subarctic (2) or savanna (3) climate. Finally, six sandy grid cells are located under tropical (2), desertic (2) or semiarid (2) climate (Tables 1 and 2). In this study, the grid cells are referred as warm environments where the mean annual temperature is above 18°C, and cold environments apply to grid cells where the mean annual temperature is always below 11°C.

4.2. Data

[20] Climate data over the study sites are provided by CRU-TS 2.1 spatial climate data set with a spatial resolution of 0.5° latitude versus 0.5° longitude [*New et al.*, 2000; *Mitchell and Jones*, 2005]. This data set includes monthly air temperature, precipitation, cloud cover and amount of wet days for the 1901–2002 period. The annual mean temperature and precipitation are reported in Table 2. Soil information including textural fraction (clay, silt, sand % abundance), bulk density (kg m^{-3}), coarse fraction (%) and porosity are taken from the ISRIC-WISE global data set [*Batjes*, 2005]. Lithological information used to fix the mineralogy of the saprolitic layer is provided by a global rock lithology database (1° latitude versus a 1° longitude) [*Amiotte-Suchet et al.*, 2003]. The definition of soil types is based on the HWSD data set [*Food and Agriculture Organization* (*FAO*), 2008], itself based on a compilation of four databases: the European Soil Database (version 2.0, European Soil Bureau, Ispra, Italy, 2004), the 1:1,000,000 soil map of China [*Shi et al.*, 2004], various regional SOTER databases (SOTWIS Database) and the Soil Map of the World [*FAO,* 1971, 1995].

[21] The B-WITCH model is forced with constant rain compositions of K^+ (4.03×10^{-6} mol L^{-1}), Mg^{2+} (0.62×10^{-6} mol L^{-1}), Ca^{2+} (4.97×10^{-6} mol L^{-1}) and SO_4^{2-} (7.61×10^{-6} mol L^{-1}) over the 22 grid cells in order to limit the number of variable parameters.

4.3. Mineralogical Composition of Soils and Rocks

[22] Based on these global data sets, the mineralogical compositions of surficial and medium soil layers are defined from the soil type and evolution, and the deep saprolitic layer composition. Based on previous studies, a precise mineralogical composition is defined according to the soil type (Table 1). For three grid cells, a distinct method is used. These grid cells are located in China (grid cell 17), Venezuela (grid cell 7) and Ethiopia (grid cell 9) and are referenced as cambic arenosol, dystric regosol and lithic leptosol, respectively. Since, these soils are not well developed, their mineralogical composition is assumed to be similar to the underlying bedrock composition.

Table 1. Soil Characteristic of the 22 Modeled Grid Cells[a]

Grid Cell Location	Grid Cell	Continent	Bedrock	Soil Types	Minerals in Layer 1	Minerals in Layer 2	References
30°75′S, 119°25′E	1	Australia	basalt	calcic luvisol	Qz, K, chl (bio, Ca-Mont)	K, chl (bio, Qz, Ca-Mont)	*Mokma et al.* [1973], *Beckmann et al.* [1974]
25°25′S, 54°75′W	2	South America	basalt	plinthic acrisol	K, Qz, gib	K, Qz, gib	*Cornu et al.* [1998], *Dalmolin et al.* [2006]
24°25′S, 52°75′W	3	South America	basalt	rhodic ferralsol	K, Qz, gib	K, Qz, gib	*Cornu et al.* [1998], *Dalmolin et al.* [2006]
10°25′S, 69°25′W	4	South America	sand	haplic acrisol	Qz, K, gib	Qz, K, gib	*Fritsch et al.* [2007]
10°25′S, 52°75′W	5	South America	sand	dystric gleysol	Qz, alb, ort, ill, Ca-Mont (K, chl)	Qz, ort, alb, Ca-Mont, ill (K, chl)	*Wiseman and Püttmann* [2006]
2°75′N, 27°25′E	6	Africa	granite	orthic ferralsol	Qz, gib, K	Qz, gib, K	*Reatto et al.* [2009]
4°25′N, 62°25′W	7	South America	granite	dystric regosol	and, Qz, ort, bio, hor (apa)	and, Qz, ort, bio, hor (apa)	
8°25′N, 3°75′W	8	Africa	granite	plinthic acrisol	Qz, K, gib	Qz, K, gib (bio)	*Peinemann et al.* [2000]
10°25′N, 40°25′E	9	Africa	basalt	lithic leptosol	lab, dio, bas.glass (apa, for)	lab, dio, bas.glass (apa, for)	
16°75′N, 79°75′E	10	Asia	granite	chromic luvisol	Qz, ort, and, ill (K, chl)	Qz, ill, ort, and (K, chl)	*Rühlmann et al.* [2006]
17°75′N, 82°25′E	11	Asia	granite	eutric nitosol	Qz, K, ill	Qz, K, ill	*Fritsch et al.* [2007]
20°25′N, 77°75′E	12	Asia	basalt	chromic vertisol	Ca-Mont, K, ill, Qz (chl, lab)	Ca-Mont, K, ill, Qz (chl, lab)	*Pharande and Sonar* [1997]
20°75′N, 75°75′E	13	Asia	basalt	chromic vertisol	Ca-Mont, K, ill, Qz (chl, lab)	Ca-Mont, K, ill, Qz (chl, lab)	*Pharande and Sonar* [1997]
41°25′N, 113°25′W	14	North America	sand	orthic solonetz	Qz (Ca-Mont, K, ill)	Qz, Ca-Mont (K, ill)	*Paquet et al.* [1966]
40°25′N, 101°75′W	15	North America	sand	luvic kastanozem	Qz, ort, chl, ill, Ca-Mont, cal	Qz, chl, ill, Ca-Mont (ort, cal)	*Sanchez-Maranon et al.* [2004], *Schwanghart and Schütt* [2008]
42°75′N, 110°75′E	16	Asia	sand	luvic calcisol	Qz, cal, K, chl	Qz, cal, K, chl	*Malicki et al.* [1996]
42°75′N, 121°25′E	17	Asia	sand	cambic arenosol	Qz, alb, ort, K (chl)	Qz, alb, ort, K (chl)	
43°25′N, 7°75′W	18	Europe	granite	Dystric podzoluvisol	K, mus, ill, Qz, and	K, mus, ill, Qz, and	*Galán et al.* [2007]
45°25′N, 3°75′E	19	Europe	basalt	andosol	Dio, lab, K, Ca-Mont, Qz (for)	dio, lab, K, Ca-Mont (Qz, for)	*Bonfils and Moinereau* [1971], *Feijtel et al.* [1989]
50°75′N, 104°25′E	20	Asia	granite	dystric gleysol	Qz, ort, and, ill, Ca-Mont (K, chl)	Qz, ort, and, ill, Ca-Mont (K, chl)	*Wiseman and Püttmann* [2006]
50°75′N, 113°75′E	21	Asia	granite	eutric cambisol	Qz, ort, ill (and, K, chl)	Qz, ort, ill (and, K, chl)	*Rühlmann et al.* [2006]
60°75′N, 100°25′E	22	Asia	basalt	gelic gleysol	Ca-Mont, Qz, ort, chl (and)	Ca-Mont, Qz, ort, chl (and)	*Pokrovsky et al.* [2005]

[a]Geographical coordinates in degrees and soil type from the HWSD data set [*FAO*, 2008]. Table 1 also provides the dominant (descending order of abundance) and minor (less than 5% vol, within parentheses) minerals in layers 1 and 2 and references for soil mineralogical composition for surficial and medium layers. Qz, quartz; K, kaolinite; chl, chlorite; bio, biotite; Ca-Mont, Ca-montmorillonite; gib, gibbsite; and, andesine; ort, orthose; ill, illite; lab, labradorite; bas.glass, basaltic glass; alb, albite; mus, muscovite; cal, calcite; for, forsterite; dio, diopside; apa, apatite; hor, hornblend.

Table 2. Characteristic of Each Grid Cell[a]

Grid Cell Location	Grid Cell	Continent	Country	Climate	T (°C)	P (mm yr^{-1})
30°75′S, 119°25′E	1	Australia	Australia	Semiarid	18.5	316.53
25°25′S, 54°75′W	2	South America	Paraguay	Humid subtropical	21.5	1689.78
24°25′S, 52°75′W	3	South America	Brazil	Humid subtropical	20	1677.81
10°25′S, 69°25′W	4	South America	Brazil	Tropical	25.8	1645.92
10°25′S, 52°75′W	5	South America	Brazil	Tropical	26	1720.38
2°75′N, 27°25′E	6	Africa	DR Congo	Tropical	23.9	1496.55
4°25′N, 62°25′W	7	South America	Venezuela	Tropical	24.1	2714.86
8°25′N, 3°75′W	8	Africa	Ivory Coast	Savanna	27.1	1001.7
10°25′N, 40°25′E	9	Africa	Ethiopia	Semiarid	25.6	606.42
16°75′N, 79°75′E	10	Asia	India	Savanna	28.8	809.67
17°75′N, 82°25′E	11	Asia	India	Savanna	25.6	1058.61
20°25′N, 77°75′E	12	Asia	India	Savanna	27.2	844.99
20°75′N, 75°75′E	13	Asia	India	Semiarid	27.2	657.81
41°25′N, 113°25′W	14	North America	USA	Desertic	10.5	252.11
40°25′N, 101°75′W	15	North America	USA	Semiarid	11	464.59
42°75′N, 110°75′E	16	Asia	China	Desertic	5.2	195.01
42°75′N, 121°25′E	17	Asia	China	Semiarid	6.6	444.36
43°25′N, 7°75′W	18	Europe	Spain	Oceanic	11.3	1428.90
45°25′N, 3°75′E	19	Europe	France	Oceanic	9.4	1220.50
50°75′N, 104°25′E	20	Asia	Russia	Subarctic	–3.2	601.49
50°75′N, 113°75′E	21	Asia	Russia	Subarctic	–1.7	301.45
60°75′N, 100°25′E	22	Asia	Russia	Subarctic	–6.8	373.94

[a]Geographical coordinates, continent, country, climate, and mean annual temperature and precipitation over 1982–2002 period provided by CRU-TS 2.1 spatial climate data set [*New et al.*, 2000; *Mitchell and Jones*, 2005].

[23] Finally, the mineralogical composition of layer 3 (saprolitic layer) is summarized in Table 3 [*Best*, 2003].

5. Results and Discussion

5.1. Spatial Distribution of Vegetation

[24] As mentioned above, rising atmospheric CO_2 impacts the stomatal conductance and the biome distribution. We first discuss the influence of the CO_2 increase on the predicted vegetation type distribution for each grid cell. These results can be seen as additional information at the regional scale to the results of the global analysis performed by *Leipprand and Gerten* [2006].

[25] In grid cells where the annual mean temperature is between 5°C and 11°C, the predominant temperate herbaceous PFT are replaced by evergreen or summergreen temperate PFTs (4 grid cells) with a CO_2 concentration rise (Figure 3a). In grid cells with an annual mean temperature below 5°C, the predominant evergreen PFTs (nondeciduous forest) are progressively replaced by summergreen PFT (deciduous forest) with CO_2 concentrations rising from 280 to 1120 ppmv (Figure 3b). This is consistent with the results from [*Mickler et al.*, 2002] who have modeled the net primary productivity (NPP) of evergreen and deciduous forest in USA from 1992 to 2050. Testing a climate warming scenario, they show an increase in the deciduous NPP by about 24% between 1992 and 2050 while the evergreen NPP rises only by 2%.

[26] Regarding the so-called warm grid cells where the annual mean temperature is around 25°C and rainfall above 1500 mm yr^{-1} (6 grid cells), the dominant tropical evergreen PFTs are progressively replaced by tropical raingreen PFTs (deciduous forest) with increasing CO_2 concentration (Figure 3c). Although the evergreen PFT is characterized by a more important net productivity (around 2000 g C m^{-2}), the raingreen PFT is more sensitive to the CO_2 rise in the LPJ model, leading to the progressive replacement of the evergreen PFT by the raingreen one. In grid cells where the temperature is above to 25°C and precipitation ranges between 606 and 1058 mm yr^{-1} (6 grid cells), increased atmospheric CO_2 induces the replacement of the dominant tropical herbaceous by evergreen or raingreen PFTs (at 560 or 1120 ppmv) (Figure 3d). Indeed, the tropical herbaceous (C4 plants) assimilate more CO_2 and loose less water at low CO_2 level than C3 trees. However, when CO_2 rises, productivity of the C3 trees rises rapidly and tropical forest PFTs finally

Table 3. Soil Characteristics of the 22 Grid Cells[a]

Grid Cell Location	Grid Cell	Continent	Bedrock	Soil Types	Minerals of Saprolithe (% vol)
30°75′S, 119°25′E	1	Australia	basalt	calcic luvisol	lab (54), dio (31.2), bas.glass (9.2) (apa (4.3), for (1.3))
25°25′S, 54°75′W	2	South America	basalt	plinthic acrisol	lab (54), dio (31.2), bas.glass (9.2) (apa (4.3), for (1.3))
24°25′S, 52°75′W	3	South America	basalt	rhodic ferralsol	lab (54), dio (31.2), bas.glass (9.2) (apa (4.3), for (1.3))
10°25′S, 69°25′W	4	South America	sand	haplic acrisol	Qz (63.3), alb (10.7), ort (8.25), K (7.2) (chl (2.9))
10°25′S, 52°75′W	5	South America	sand	dystric gleysol	Qz (63.3), alb (10.7), ort (8.25), K (7.2) (chl (2.9))
2°75′N, 27°25′E	6	Africa	granite	orthic ferralsol	and (49), Qz (22), ort (16), hor (6.5), bio (6.5) (apa (0.28))
4°25′N, 62°25′W	7	South America	granite	dystric regosol	and (49), Qz (22), ort (16), hor (6.5), bio (6.5) (apa (0.28))
8°25′N, 3°75′W	8	Africa	granite	plinthic acrisol	and (49), Qz (22), ort (16), hor (6.5), bio (6.5) (apa (0.28))
10°25′N, 40°25′E	9	Africa	basalt	lithic leptosol	lab (54), dio (31.2), bas.glass (9.2) (apa (4.3), for (1.3))
16°75′N, 79°75′E	10	Asia	granite	chromic luvisol	and (49), Qz (22), ort (16), hor (6.5), bio (6.5) (apa (0.28))
17°75′N, 82°25′E	11	Asia	granite	eutric nitosol	and (49), Qz (22), ort (16), hor (6.5), bio (6.5) (apa (0.28))
20°25′N, 77°75′E	12	Asia	basalt	chromic vertisol	lab (54), dio (31.2), bas.glass (9.2) (apa (4.3), for (1.3))
20°75′N, 75°75′E	13	Asia	basalt	chromic vertisol	lab (54), dio (31.2), bas.glass (9.2) (apa (4.3), for (1.3))
41°25′N, 113°25′W	14	North America	sand	orthic solonetz	Qz (63.3), alb (10.7), ort (8.25), K (7.2) (chl (2.9))
40°25′N, 101°75′W	15	North America	sand	luvic kastanozem	Qz (63.3), alb (10.7), ort (8.25), K (7.2) (chl (2.9))
42°75′N, 110°75′E	16	Asia	sand	luvic calcisol	Qz (63.3), alb (10.7), ort (8.25), K (7.2) (chl (2.9))
42°75′N, 121°25′E	17	Asia	sand	cambic arenosol	Qz (63.3), alb (10.7), ort (8.25), K (7.2) (chl (2.9))
43°25′N, 7°75′W	18	Europe	granite	Dystric podzoluvisol	and (49), Qz (22), ort (16), hor (6.5), bio (6.5) (apa (0.28))
45°25′N, 3°75′E	19	Europe	basalt	Andosol	lab (54), dio (31.2), bas.glass (9.2) (apa (4.3), for (1.3))
50°75′N, 104°25′E	20	Asia	granite	dystric gleysol	and (49), Qz (22), ort (16), hor (6.5), bio (6.5) (apa (0.28))
50°75′N, 113°75′E	21	Asia	granite	eutric cambisol	and (49), Qz (22), ort (16), hor (6.5), bio (6.5) (apa (0.28))
60°75′N, 100°25′E	22	Asia	basalt	gelic gleysol	lab (54), dio (31.2), bas.glass (9.2) (apa (4.3), for (1.3))

[a]Geographical coordinates in degrees, continent, bedrock, soil type provided by HWSD data set and dominant and minor minerals for the deep saprolitic layer [*Best*, 2003]. Qz, quartz; K, kaolinite; chl, chlorite; bio, biotite; and, andesine; ort, orthose; lab, labradorite; bas.glass, basaltic glass; alb, albite; for, forsterite; dio, diopside; apa, apatite; hor, hornblend.

overcome tropical herbaceous PFT [*Kimball et al.*, 1993].

5.2. Hydrologic Cycle: Evapotranspiration, Runoff, and Drainage

[27] Many studies have already highlighted the effect of atmospheric CO_2 increase on the continental water cycle, including both freshwater discharge and evapotranspiration.

[28] The rise of atmospheric CO_2 over the last century has probably led to an increase in runoff, through reduced transpiration, according to *Probst and Tardy* [1989], *Labat et al.* [2004], and *Gedney et al.* [2006]. However, the existence of a significant trend (positive or negative) in freshwater discharge to oceans and the influence of climate change on freshwater discharge remain under debate and depend on the method used to evaluate the rate of changes, e.g., model versus data-based estimations

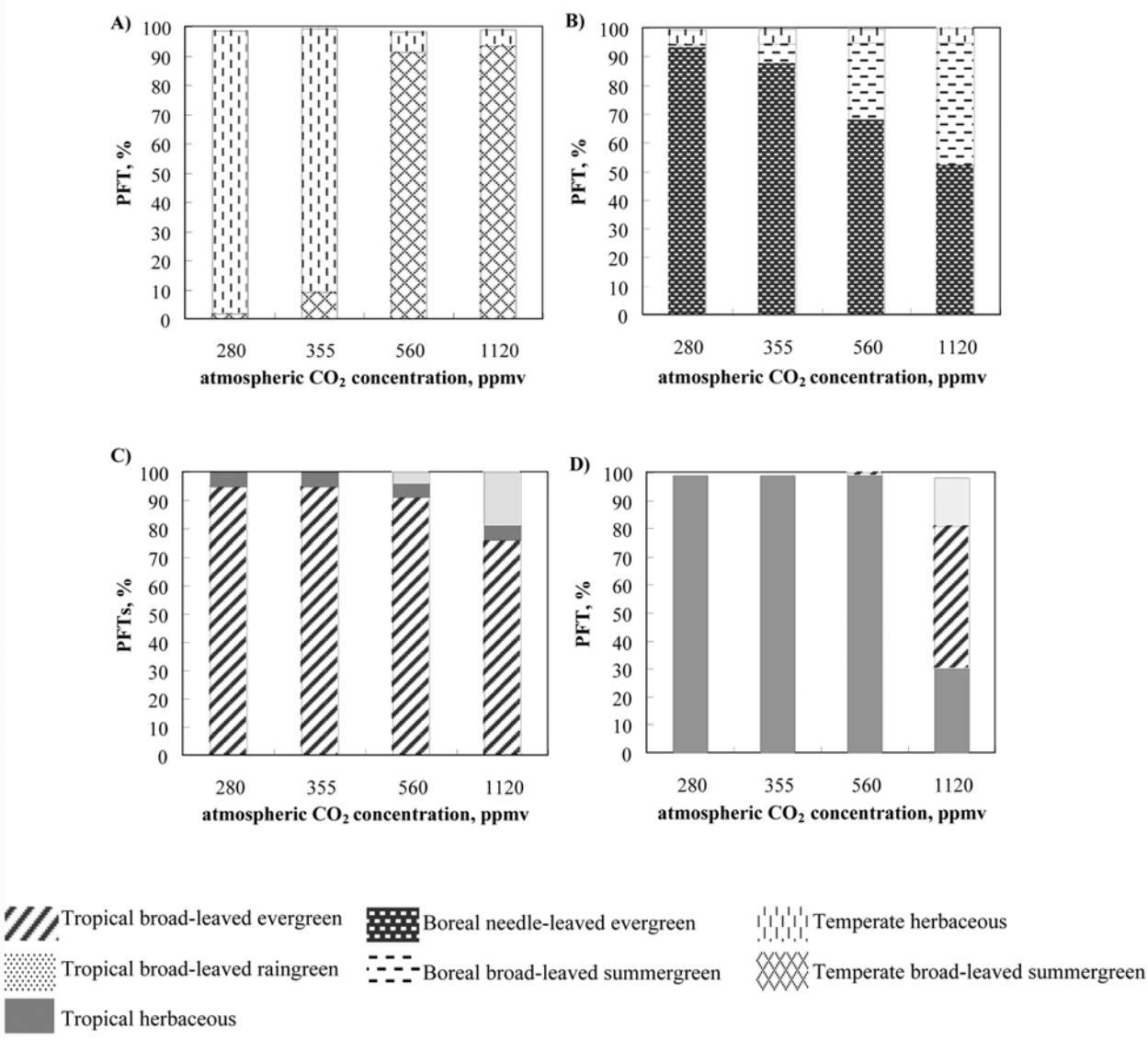

Figure 3. Cover percentage of plant functional types (PFT) as a function of atmospheric CO_2 concentration in ppmv on grid cells located (a) in the United States (North America, grid cell 15) on sandy rock, (b) in Russia (Asia, grid cell 20) on granitic rock, (c) in DR Congo (Africa, grid cell 6) on granitic rock, and (d) in Ethiopia (Africa, grid cell 9) on basaltic rock.

[*Dai et al.*, 2009]. The effects of CO_2 changes on evapotranspiration have already been investigated by *Friend and Cox* [1995] and *Kruijt et al.* [2008], who show a reduction between 15% and 25% with CO_2 concentration ranging from 355 to 700 ppmv, which would promote an increase in the discharge of fresh water to the ocean.

[29] In the present study, the LPJ simulations for the 22 grid cells yield similar results for most of the grid cells. The atmospheric CO_2 increase implies a decrease in the evapotranspiration and an increase in the drainage and surficial runoff for atmospheric CO_2 concentration ranging from 280 ppmv to 1120 ppmv (Figures 4a–4d). In warm environments (mean annual temperature above 11°C), evapotranspiration decreases by about 6%, the drainage and the surficial runoff increase by about 14% and 9%, respectively, from present-day CO_2 pressure up to a fourfold increase. In cold environments (mean annual temperature below 11°C), evapotranspiration decreases by about 14% and the drainage and the surficial runoff increase by about 24% and 17%, respectively. However, a few grid cells yield different results. The change in the hydrologic behavior

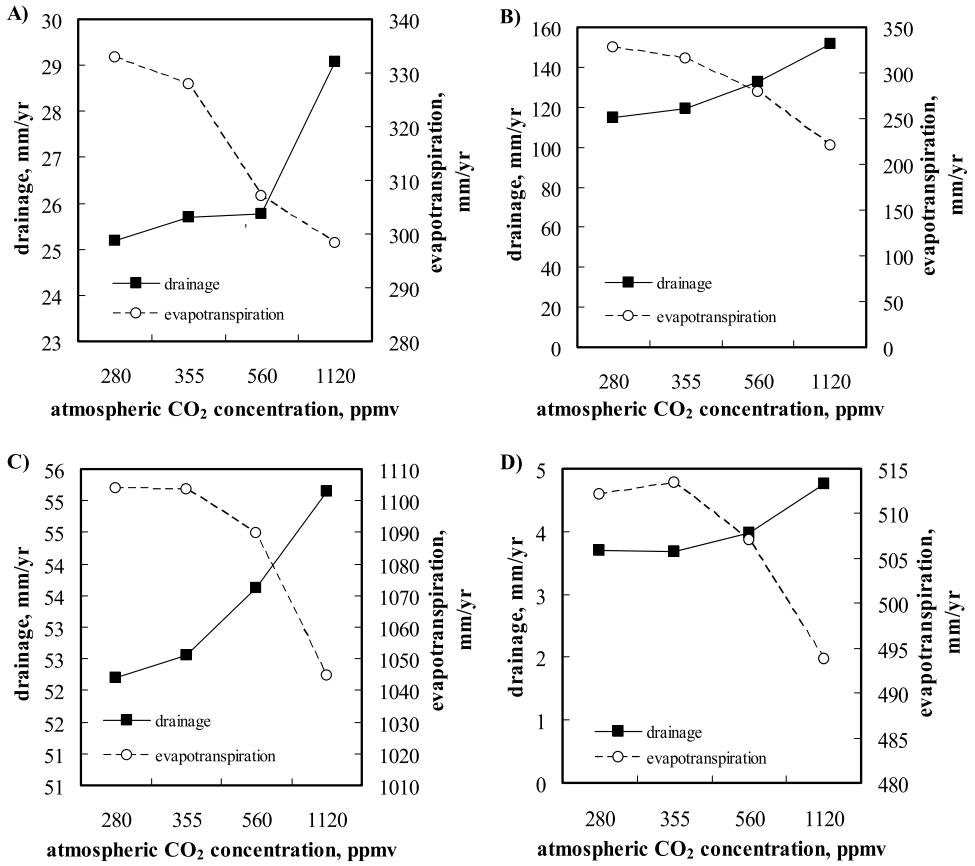

Figure 4. Vertical drainage and evapotranspiration in mm yr^{-1} versus atmospheric CO_2 concentration in ppmv. The evapotranspiration and drainage are calculated by LPJ on grid cells located (a) in the United States (North America, grid cell 15) on sandy rock, (b) in Russia (Asia, grid cell 20) on granitic rock, (c) in DR Congo (Africa, grid cell 6) on granitic rock, and (d) in Ethiopia (Africa, grid cell 9) on basaltic rock.

not only depends on the stomatal closure, but also responds to the change in the potential vegetation. The evapotranspiration strongly increases (170%) and the drainage and runoff decrease by 84% and 54% for the grid cell located in USA (grid cell 14). The same result is observed for the grid cell in China (grid cell 16) where the evapotranspiration increases by 180% and drainage and runoff decrease by 94% and 66%. The vegetation fractional cover of these grid cells increases with atmospheric CO_2. Indeed, the temperate herbaceous cover fraction doubles from 280 to 1120 ppmv for the USA grid cell and increases by 21% from 280 to 560 ppmv for the Chinese grid cell. This is in agreement with *Leipprand and Gerten* [2006] who have found a vegetation fractional cover rise for a CO_2 doubling for these regions. The drainage and the evapotranspiration for three Indian grid cells (10, 12, and 13) and for the Ethiopian grid cell (9) remain stable between 280 and 560 ppmv. At both CO_2 levels, 100% of the grid cells are occupied by the tropical herbaceous PFT. Moreover, these grid cells are extremely dry: local rainfall is twice to three times lower than rainfall in the other warm environments. The resulting drainage is very low, below 5 mm yr^{-1} and soil water content in the superficial and medium soil layers stays close to zero. Then, a part of tropical herbaceous is replaced by tropical raingreen or evergreen PFTs, and the resulting evapotranspiration and drainage decrease and increase, respectively, between 560 and 1120 ppmv.

[30] Over the grid cells in Paraguay (grid cell 2) and in Brazil (grid cell 3) the drainage decreases by about 35% for a CO_2 concentration rising from 280 to 355 ppmv because the temperate evergreen forest replaces the temperate herbaceous. This drainage decrease is the result of an enhanced uptake of water by the trees. The evapotranspiration increases over the two grid cells. The vegetal cover then stabilizes, and the evapotranspiration starts decreasing and the

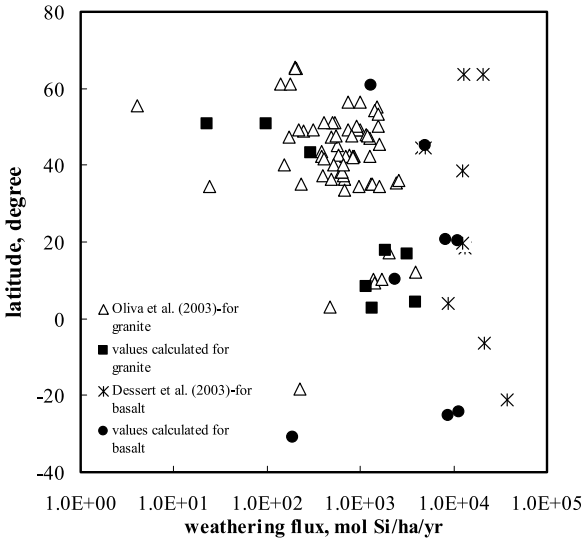

Figure 5. Latitude in degrees versus weathering flux in mol Si ha^{-1} yr^{-1}. The weathering fluxes calculated by B-WITCH model on granitic (solid squares) and basaltic (solid circles) rock are compared to field data from *Oliva et al.* [2003] for granitc monolithological watersheds (open triangles) and from *Dessert et al.* [2003] for basaltic watersheds (stars).

drainage increases for simulations with atmospheric CO_2 above 355 ppmv.

[31] In summary, the standard hydrological behavior is an increase in the vertical drainage of the soil and saprolite when atmospheric CO_2 rises as a result of a progressive stomatal closure. However, the LPJ model also predicts the replacement of some PFTs by others when CO_2 rises, partly hiding the stomatal closure effect and introducing specific behaviors (including a decrease of drainage with rising CO_2) for a few grid cells (2 grid cells among 22).

5.3. Weathering Fluxes and CO_2 Consumption Rates

5.3.1. Validation of the Model for Atmospheric CO_2 Concentration of 355 ppmv

5.3.1.1. Silica Weathering Flux

[32] The weathering flux for a given grid cell (export to the river) is calculated as the sum of two terms: the surficial runoff times the calculated element concentration in the upper layer and the deep vertical drainage times the calculated concentration in the deep saprolitic layer. Under 355 ppmv of CO_2 and with the observed climate from the CRU, the calculated silica flux ranges from 190.54 (Australia, grid cell 1) to 11360 mol Si ha^{-1} yr^{-1} (Brazil, grid cell 3) for the basaltic lithology, from 22.58 (Russia, grid cell 21) to 3852.70 mol Si ha^{-1} yr^{-1} (Venezuela, grid cell 7) for the granitic lithology, and from 22.34 (China, grid cell 17) to 420.73 mol Si ha^{-1} yr^{-1} (Brazil, grid cell 5) for the sandy rock lithology.

[33] For validation purposes, the calculated silica flux release by weathering reactions for basaltic and granitic lithologies at 355 ppmv are compared with the data from *Oliva et al.* [2003] and *Dessert et al.* [2003] (Figure 5). Both studies report weathering flux for granitic and basaltic monolithological catchments, respectively, under a large variety of climates. The measured silica flux for granitic catchments fluctuates from 4 to 8066 mol ha^{-1} yr^{-1} [*Oliva et al.*, 2003] and from 4535 to 122142 mol ha^{-1} yr^{-1} for basaltic catchments [*Dessert et al.*, 2003]. The range of calculated values falls within the observed range for both lithologies. When plotting the calculated and observed silica flux as a function of latitude (Figure 5), a general agreement between both set of points is obtained. They both display a general increase in the silica flux from the pole to the equator in the Northern Hemisphere, particularly for granitic lithologies. The increase in the weathering flux toward the equator is mainly driven by the increase in runoff by an order of magnitude and by the rise in temperatures. But Figure 5 also shows that the increasing rate of the weathering flux with latitude is at maximum at high latitude (above 40°N), and tends toward zero at low latitude (below 40°N). Between about 60 and 40°N, both the model and data show an increase in the weathering fluxes by more than two order of magnitudes, while it spans only one order of magnitude from 40°N to the equator. No clear trend can be inferred from the observations and from the calculations for the Southern Hemisphere, due to the limited number of points. Calculated silica flux for granitic lithologies display a general increasing trend with runoff. However, the spreading of the calculated fluxes is important. This is also the case for the field data (Figure 6). For basaltic lithologies, a sharp increase with runoff is simulated by B-WITCH, extending the data points from *Dessert et al.* [2003] into the low runoff values (Figure 7).

5.3.1.2. River Cation Concentrations

[34] Calculated river cation and bicarbonate concentrations (355 ppmv) are also compared to the data from *Oliva et al.* [2003] and *Dessert et al.* [2003] for both the granitic and basaltic lithologies. River

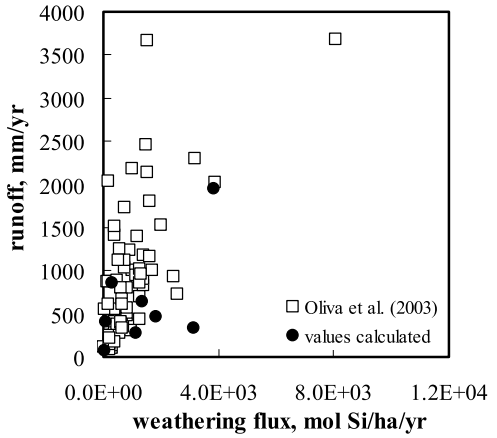

Figure 6. Runoff in mm yr^{-1} versus weathering flux in mol Si ha^{-1} yr^{-1} for granitic grid cells. The runoff is calculated by LPJ, and weathering flux is calculated by WITCH (solid circles). Field data from *Oliva et al.* [2003] (open squares).

concentrations for a given species C_{riv} is calculated as follows:

$$C_{riv} = \frac{R_{surf} \cdot C_1 + D \cdot C_3}{R_{surf} + D} \quad (5)$$

where R_{surf} is the surficial runoff calculated by LPJ for each grid element, D is the deep drainage, C_1 and C_3 are the concentration of the species in the surficial soil layer and in the saprolite, respectively [*Roelandt et al.*, 2010].

[35] The mean annual calculated river cation concentrations range from 87 to 244 μmol L^{-1} for the granitic lithology. Calculated riverine bicarbonate concentrations range from 277 to 2539 μmol L^{-1} for the basaltic lithology. These values are consistent with the literature data (from 7 to 715 μmol L^{-1} at the outlet of granitic watersheds and 354 to 2719 μmol L^{-1} for basaltic watersheds). The B-WITCH model is thus able to match the general features of the present-day weathering processes, particularly the CO_2 consumption.

5.3.1.3. Lithological Control of the Weathering Fluxes at 355 ppmv of CO_2

[36] The highest weathering fluxes are simulated for the basaltic lithologies while the sandy lithologies display the lowest fluxes. Weathering fluxes are thus directly related to the weatherability of the constitutive minerals for each lithology. For the basaltic lithology, the weathering products are supplied by the dissolution of diopside and labradorite. Andesine dissolution is the main provider of dissolved species for the granitic lithology and albite for the sandy rocks.

[37] There is a strong temperature control for the three lithologies (Figure 8a): weathering fluxes are predicted to be higher under warm climates. The dependence of the weathering fluxes on runoff display a more complex pattern. For basaltic lithologies, fluxes increase with runoff until about 300 mm yr^{-1}. Above this value, weathering fluxes saturate at a maximum value around 10^4 mol Si ha^{-1} yr^{-1}. For sandy lithologies, weathering rates increase over the all simulated runoff range (up to 800 mm yr^{-1}). However, there is no simulated sites displaying runoff between 150 and 650 mm yr^{-1}. This gap might possibly hide an inflexion point. Weathering fluxes for granitic lithologies display a complex pattern. Whether it saturates around 300 mm yr^{-1} is unclear due to the too low number of simulated sites. The saturation effect has been previously documented by *Bluth and Kump* [1994] from the compilation of the weathering fluxes measured in the field. Here, the drainage is higher for high-runoff sites, thus promoting mineral dissolution rates and increasing weathering rates. But the simulated weathering system shift toward a weathering limited regime around 300 mm yr^{-1} for basaltic lithologies, and possibly for granitic lithologies too.

[38] Finally, *Dessert et al.* [2003] have compiled the CO_2 consumption rate for different watersheds located in tropical and boreal environments. This rate varies from 0.30×10^6 mol C km^{-2} yr^{-1} (Massif Central, France) to 6.40×10^6 mol C km^{-2} yr^{-1} (Java, Indonesia). So, these values are very close to

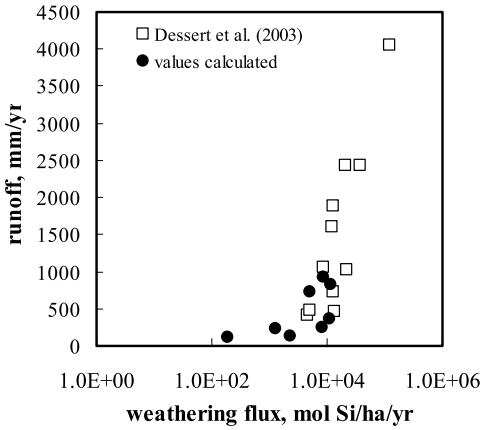

Figure 7. Runoff in mm yr^{-1} versus weathering flux in mol Si ha^{-1} yr^{-1} on basaltic rock. The runoff is calculated by LPJ, and weathering flux is calculated by WITCH (solid circles). Field data from *Dessert et al.* [2003] (open squares).

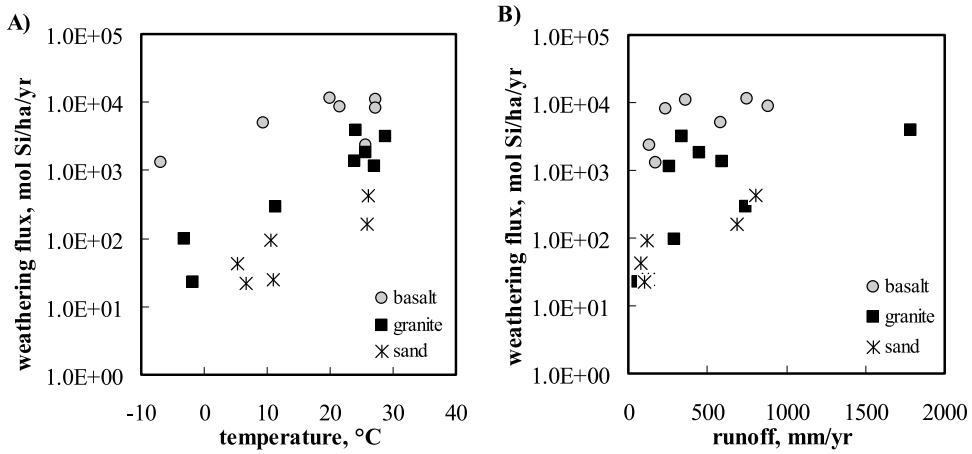

Figure 8. Calculated weathering flux in mol Si ha^{-1} yr^{-1} (a) versus temperature in degrees Celsius and (b) versus runoff in mm yr^{-1} for basaltic (gray circles), granitic (solid squares), and sandy (stars) lithologies. The temperature is the mean value over the 1982–2002 period, and the runoff is calculated by the LPJ model.

ones calculated with coupling LPJ-WITCH, ranging from 0.03×10^6 (grid cell 1) to 2.1×10^6 mol C km^{-2} yr^{-1} (grid cell 3).

5.3.2. Sensitivity of the Weathering Fluxes to Increased CO_2

[39] The dependence of CO_2 consumption by silicate weathering as a function of atmospheric CO_2 levels has been previously quantified within the framework of the geological carbon cycle evolution. In the presence of vascular land plants, this dependence is written as follows [*Berner and Kothavala*, 2001; *Berner*, 2004]:

$$F_{CO2} = \left(\frac{2R_{CO2}}{1 + R_{CO2}}\right)^{0.4} \quad (6)$$

where R_{CO2} is the ratio of the partial pressure of atmospheric CO_2 to the preindustrial value ($R_{CO2} = 1$ for the preindustrial state). F_{CO2} is called the fertilization factor as it accounts for the enhanced biological impact on weathering as CO_2 rises ($F_{CO2} = 1$ for the preindustrial state) [*Berner*, 2004]. Mathematically speaking, F_{CO2} is a multiplier of the silicate weathering rate. This Michaelis-Menten type law allows the limitation of the fertilization effect at very high CO_2 levels due to the progressive lack of nutrients. For atmospheric CO_2 levels ranging from 280 to 1120 ppmv, this limitation effect is not operating and F_{CO2} roughly displays a linear rise with a slope of 2% increase in weathering per 100 ppmv rise in CO_2. As mentioned by *Berner* [2004], this equation is used as a simple first approximation for a process that is poorly understood.

[40] Here we provide a first quantitative estimation of this fertilization effect on the silicate weathering rates. In the present B-WITCH simulations, the sensitivity to CO_2 changes might be higher by up to a factor of 2 (Figure 9a). Many grid elements display a 2.4% to 5% increase in weathering per 100 ppmv rise at steady state. This CO_2 consumption rise is driven by the enhanced drainage as the stomatal closure inhibits the evapotranspiration, and by the rise in below ground CO_2 levels, itself driven by the fertilization effect.

[41] Overall, the CO_2 consumption above granitic and basaltic rocks increases by an average of 25% for CO_2 rising from 280 to 1120 ppmv (3% per 100 ppmv), for grid cells where an increase is predicted by the model. However, the standard deviation is close to 10%, illustrating the variability in the sensitivity to the CO_2 change. Indeed, our results suggest that there is no unequivocal latitudinal, temperature, rainfall, vegetation type, nor lithological dependence of this rate of increase. 60% of this increase is related to the evapotranspiration decrease and concomittant drainage increase. The remaining 40% increase is linked to soil CO_2 rise driven by the fertilization effect.

[42] Finally, the response of the CO_2 consumption through silicate weathering to enhanced CO_2 also depends on the possible vegetation change, and not only on the stomatal closure at high CO_2. For instance, grid cell 2 in Paraguay and grid cell 3 in Brazil display first a decrease in the CO_2 consumption between 280 and 355 ppmv (Figure 9b). This decrease is related to a potential vegetation change, from temperate herbaceous to temperate

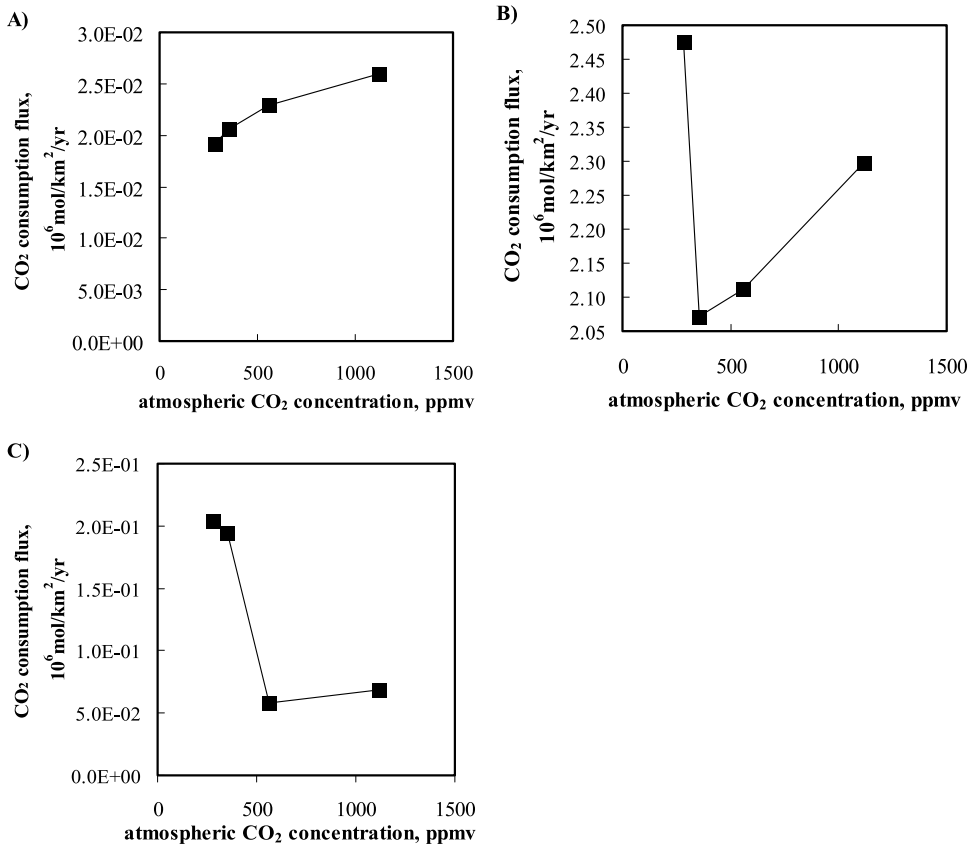

Figure 9. Calculated CO_2 consumption flux in 10^6 mol km^{-2} yr^{-1} versus atmospheric CO_2 concentration in ppmv, on grid cells located (a) in Russia (grid cell 21) on granitic rock, (b) in Brazil (grid cell 3) on basaltic rock, and (c) in China (grid cell 16) on sandy rock.

broad-leaved evergreen PFT, inducing a strong decrease in the drainage by about 30% which impacts on the dissolution rates. Once this potential vegetation change is achieved (above 355 ppmv) CO_2 consumption starts to rise again with CO_2. The dominant vegetation functional type remains constant and stomatal closure again controls the vertical drainage increase. Grid cells 14 (USA) and 16 (China) display a strong decrease (factor of 4) in the CO_2 consumption flux with rising CO_2 concentration from 280 to 1120 ppmv (Figure 9c). Over these grid cells, the vegetated surface cover increases with CO_2 (fertilization effect) and the drainage continuously decreases over the range of tested CO_2 atmospheric concentration.

6. Conclusions and Perspectives

[43] In this contribution, we explore the impact of atmospheric CO_2 concentration (from 280 to 1120 ppmv) on continental silicate weathering through changes in continental vegetation and drainage. The B-WITCH model estimates the vegetation dynamics, water and CO_2 fluxes and weathering reactions in soil and saprolite. B-WITCH is run for 22 sites located all over the world for which mineralogical compositions have been reconstructed, covering a wide range of climatic and lithologic conditions. All simulations are run until a steady state is reached for a variety of atmospheric CO_2 pressures, keeping other climate forcings constant.

[44] Our results show that, under 355 ppmv of atmospheric CO_2, B-WITCH is able to reproduce the global pattern of weathering rates as a function of either annual runoff, mean annual temperature or latitude for various lithologies (basaltic and granitic).

[45] In agreement with previous studies, we calculate that the increase in atmospheric CO_2 concentrations induces changes in the vegetal cover, a general increase in the vertical drainage of the soil and saprolite up to 20% and a decrease in evapotranspiration rate up to 22% in response to stomatal closure. As a result of the drainage increase, the

B-WITCH model predicts for most of the simulated sites, an increase in the CO_2 consumption through continental silicate weathering by 2.4% to 5% per 100 ppmv increase in CO_2, suggesting a higher sensitivity of weathering than previously expected. This finding reinforces the strength of the negative feedback loop stabilizing the Earth climate at the geological time scale.

[46] However, some peculiar behaviors are identified, particularly when the vegetated fractional cover increases and when plant functional type replacement is predicted. For these sites, the vertical drainage decreases as well as the CO_2 consumption by silicate weathering flux. This modeling study thus demonstrates that CO_2 consumption through continental silicate weathering is sensitive to the atmospheric CO_2 concentration, considered as an independent parameter, through induced changes in the vegetal cover and soil water balance.

[47] Future work should account for concomittant climatic change. Non–steady state simulations must also be performed to simulate the impact of the ongoing climate change and CO_2 rise on the continental weathering. Process-based models, such as the B-WITCH model, are powerful tools to achieve such goals.

Acknowledgments

[48] This work has been funded by the EC2CO project "Les processus d"altération continentale à grande échelle: Modélisation appliquée au cas du bassin de la Mac Kenzie' and by the French National Agency for Research (ANR) project NT05-3/43171. Didier Gazen (Laboratoire d'Aérologie, Toulouse) is greatly acknowledged for the maintenance of the cluster of PC at LMTG, and Christine Delire (Météofrance, Toulouse) is acknowledged for fruitful discussions and comments on an early version of this manuscript. The anonymous reviewers and Editor Louis Derry are greatly acknowledged for their careful and constructive reviews that contributed to improve the original manuscript.

References

Amiotte-Suchet, P., and J.-L. Probst (1993), Modelling of atmospheric CO_2 consumption by chemical weathering of rocks: Application to the Garonne, Congo and Amazon basins, *Chem. Geol.*, *107*, 205–210, doi:10.1016/0009-2541(93)90174-H.

Amiotte-Suchet, P., J.-L. Probst, and W. Ludwig (2003), Worldwide distribution of continental rock lithology: Implications for atmospheric/soil CO_2 uptake by continental weathering and alkalinity river transport to the oceans, *Global Biogeochem. Cycles*, *17*(2), 1038, doi:10.1029/2002GB001891.

Batjes, N. H. (2005), ISRIC-WISE global data set of derived soil properties on a 0.5 by 0.5 degree grid (version 3.0), *Rep. 2005/02*, ISRIC-World Soil Inf., Wageningen, Netherlands.

Beckmann, G. G., C. H. Thompson, and G. D. Hubble (1974), Genesis of red and black soils on basalt on the Darling Downs, Queensland, Australia, *J. Soil Sci.*, *25*, 265–281, doi:10.1111/j.1365-2389.1974.tb01123.x.

Berner, R. A. (2004), *The Phanerozoic Carbon Cycle: CO_2 and O_2*, 150 pp., Oxford Univ. Press, New York.

Berner, R. A., and Z. Kothavala (2001), GEOCARB III: A revised model of atmospheric CO_2 over Phanerozoic time, *Am. J. Sci.*, *301*, 182–204, doi:10.2475/ajs.301.2.182.

Best, M. G. (2003), *Igneous and Metamorphic Petrology*, 752 pp., Blackwell Sci., Malden, Mass.

Bluth, G. J. S., and L. R. Kump (1994), Lithologic and climatologic control of river chemistry, *Geochim. Cosmochim. Acta*, *58*, 2341–2359, doi:10.1016/0016-7037(94)90015-9.

Bonan, G. (2002), *Ecological Climatology—Concepts and Applications*, Cambridge Univ. Press, Cambridge, U. K.

Bonfils, P., and J. Moinereau (1971), Propriétés physiques des Andosols et des sols bruns andiques au sud du Massif Central, *Cah. O. R. S. T. O. M., Ser. Pedol.*, *IX*, 345–363.

Calmels, D., J. Gaillardet, A. Brenot, and C. France-Lanord (2007), Sustained sulfide oxidation by physical erosion processes in the Mackenzie River basin: Climatic perspectives, *Geology*, *35*, 1003–1006, doi:10.1130/G24132A.1.

Cornu, S., Y. Lucas, J. P. Ambrosi, and T. Desjardins (1998), Transfer of dissolved Al, Fe and Si in two Amazonian forest environments in Brazil, *Eur. J. Soil Sci.*, *49*, 377–384, doi:10.1046/j.1365-2389.1998.4930377.x.

Dai, A., T. Qian, K. E. Trenberth, and J. D. Milliman (2009), Changes in continental freshwater discharge from 1948 to 2004, *J. Clim.*, *22*, 2773–2792, doi:10.1175/2008JCLI2592.1.

Dalmolin, R. S. D., C. N. Gonçalves, D. P. Dick, H. Knicker, E. Klamt, and I. Kogel-Knabner (2006), Organic matter characteristics and distribution in Ferralsol profiles of a clinosequence in southern Brazil, *Eur. J. Soil Sci.*, *57*, 644–654, doi:10.1111/j.1365-2389.2005.00755.x.

Dessert, C., B. Dupré, J. Gaillardet, L. M. François, and C. J. Allègre (2003), Basalt weathering laws and the impact of basalt weathering on the global carbon cycle, *Chem. Geol.*, *202*, 257–273, doi:10.1016/j.chemgeo.2002.10.001.

Donnadieu, Y., R. Pierrehumbert, R. Jacob, and F. Fluteau (2006), Modelling the primary control of paleogeography on Cretaceous climate, *Earth Planet. Sci. Lett.*, *248*, 426–437, doi:10.1016/j.epsl.2006.06.007.

Eyring, H. (1935), The activated complex in chemical reactions, *J. Chem. Phys.*, *3*, 107–115, doi:10.1063/1.1749604.

Feijtel, T. C., A. G. Jongmans, and J. D. J. van Doesburg (1989), Identification of clay coatings in an older Quaternary terrace of the Allier, Limagne, France, *Soil Sci. Soc. Am. J.*, *53*, 876–882.

Field, C. B., R. B. Jackson, and H. A. Mooney (1995), Stomatal responses to increased CO_2: Implications from the plant to the global scale, *Plant Cell Environ.*, *18*, 1214–1225, doi:10.1111/j.1365-3040.1995.tb00630.x.

Food and Agriculture Organization (FAO) (1971), The FAO-UNESCO soil map of the world, U.N. Educ., Sci., and Cult. Organ., Paris.

Food and Agriculture Organization (FAO) (1995), The digitized soil map of the world and derived soil properties, version 3.5, *Land and Water Digital Media Ser.*, *1*, Rome.

Food and Agriculture Organization (FAO) (2008), Harmonized World Soil Database, version 1.0, Rome.

Friedlingstein, P., et al. (2006), Climate-carbon cycle feedback analysis: Results from the C^4MIP model intercomparison, *J. Clim.*, *19*, 3337–3353, doi:10.1175/JCLI3800.1.

Friend, A. D., and P. M. Cox (1995), Modelling the effects of atmospheric CO_2 on vegetation-atmosphere interactions, *Agric. For. Meteorol.*, *73*, 285–295, doi:10.1016/0168-1923(94)05079-L.

Fritsch, E., A. J. Herbillon, N. R. Do Nascimento, M. Grimaldi, and A. J. Melfi (2007), From Plinthic Acrisols to Plinthosols and Gleysols: Iron and groundwater dynamics in the tertiary sediments of the upper Amazon basin, *Eur. J. Soil Sci.*, *58*, 989–1006, doi:10.1111/j.1365-2389.2006.00877.x.

Gaillardet, J., B. Dupré, P. Louvat, and C. J. Allègre (1999), Global silicate weathering and CO_2 consumption rates deduced from the chemistry of large rivers, *Chem. Geol.*, *159*, 3–30, doi:10.1016/S0009-2541(99)00031-5.

Galán, E., J. C. Fernadez-Caliani, A. Miras, P. Aparicio, and M. G. Marquez (2007), Residence and fractionation of rare earth elements during kaolinization of alkaline peraluminous granites in NW Spain, *Clay Miner.*, *42*, 341–352, doi:10.1180/claymin.2007.042.3.07.

Gedney, N., P. M. Cox, R. A. Betts, O. Boucher, C. Huntingford, and P. A. Stott (2006), Detection of a direct carbon dioxide effect in continental river runoff records, *Nature*, *439*, 835–838, doi:10.1038/nature04504.

Gerten, D., S. Schaphoff, U. Haberlandt, W. Lucht, and S. Sitch (2004), Terrestrial vegetation and water balance-hydrological evaluation of a dynamic global vegetation model, *J. Hydrol.*, *286*, 249–270, doi:10.1016/j.jhydrol.2003.09.029.

Gislason, S. R., et al. (2009), Direct evidence of the feedback between climate and weathering, *Earth Planet. Sci. Lett.*, *277*, 213–222, doi:10.1016/j.epsl.2008.10.018.

Goddéris, Y., L. M. François, A. Probst, J. Schott, D. Moncoulon, D. Labat, and D. Viville (2006), Modelling weathering processes at the catchment scale: The WITCH numerical model, *Geochim. Cosmochim. Acta*, *70*, 1128–1147, doi:10.1016/j.gca.2005.11.018.

Goddéris, Y., C. Roelandt, J. Schott, M.-C. Pierret, and L. M. François (2009), Towards an integrated model of weathering, climate, and biospheric processes, *Rev. Mineral. Geochem.*, *70*, 411–434, doi:10.2138/rmg.2009.70.9.

Gwiazda, R., and W. S. Broecker (1994), The separate and combined effects of temperature, soil pCO_2, and organic acidity on silicate weathering in the soil environment: Formulation of a model and results, *Global Biogeochem. Cycles*, *8*, 141–155, doi:10.1029/94GB00491.

Hartmann, J., N. Jansen, H. H. Dürr, S. Kempe, and P. Köhler (2009), Global CO_2-consumption by chemical weathering: What is the contribution of highly active weathering regions?, *Global Planet. Change*, *69*, 185–194, doi:10.1016/j.gloplacha.2009.07.007.

Hetherington, A. M., and F. I. Woodward (2003), The role of stomata in sensing and driving environmental change, *Nature*, *424*, 901–908, doi:10.1038/nature01843.

Hui, D., Y. Luo, W. Cheng, S. Coleman, D. W. Johnson, and D. A. Sims (2001), Canopy radiation- and water-use efficiencies as affected by elevated [CO_2], *Global Change Biol.*, *7*, 75–91, doi:10.1046/j.1365-2486.2001.00391.x.

Intergovernmental Panel on Climate Change (2007), *Climate Change 2007: The Physical Science Basis—Contribution of Working Group I to the Fourth Assessment Report of the Intergovernmental Panel on Climate Change*, Cambridge Univ. Press, Cambridge, U. K.

Kimball, B. A., J. R. Mauney, F. S. Nakayama, and S. B. Idso (1993), Effects of increasing atmospheric CO_2 on vegetation, *Vegetatio*, *104–105*, 65–75, doi:10.1007/BF00048145.

Köppen, W. (1923), *Die Klimate der Erde*, Walter de Gruyter, Berlin.

Kruijt, B., J.-P. M. Witte, C. M. J. Jacobs, and T. Kroon (2008), Effects of rising atmospheric CO_2 on evapotranspiration and soil moisture: A practical approach for the Netherlands, *J. Hydrol.*, *349*, 257–267, doi:10.1016/j.jhydrol.2007.10.052.

Labat, D., Y. Goddéris, J. L. Probst, and J. L. Guyot (2004), Evidence for global runoff increase related to climate warming, *Adv. Water Resour.*, *27*, 631–642, doi:10.1016/j.advwatres.2004.02.020.

Le Hir, G., Y. Donnadieu, Y. Goddéris, R. T. Pierrehumbert, G. P. Halverson, M. Macouin, A. Nédélec, and G. Ramstein (2009), The snowball Earth aftermath: Exploring the limits of continental weathering processes, *Earth Planet. Sci. Lett.*, *277*, 453–463, doi:10.1016/j.epsl.2008.11.010.

Leipprand, A., and D. Gerten (2006), Global effects of doubled atmospheric CO_2 content on evapotranspiration, soil moisture and runoff under potential natural vegetation, *Hydrol. Sci. J.*, *51*(1), 171–185, doi:10.1623/hysj.51.1.171.

Maher, K., C. I. Steefel, A. F. White, and D. A. Stonestrom (2009), The role of reaction affinity and secondary minerals in regulating chemical weathering rates at the Santa Cruz Soil Chronosequence, California, *Geochim. Cosmochim. Acta*, *73*, 2804–2831, doi:10.1016/j.gca.2009.01.030.

Malicki, M. A., R. Plagge, and C. H. Roth (1996), Improving the calibration of dielectric TDR soil moisture determination taking into account the solid soil, *Eur. J. Soil Sci.*, *47*, 357–366, doi:10.1111/j.1365-2389.1996.tb01409.x.

Meybeck, M. (1986), Composition chimique des ruisseaux non pollués de France, *Sci. Geol. Bull.*, *39*(1), 3–77.

Mickler, R. A., T. S. Earnhardt, and J. A. Moore (2002), Regional estimation of current and future forest biomass, *Environ. Pollut.*, *116*, S7–S16, doi:10.1016/S0269-7491(01)00241-X.

Millot, R., J. Gaillardet, B. Dupré, and C. J. Allègre (2002), The global control of silicate weathering rates and the coupling with physical erosion: New insights from rivers of the Canadian Shield, *Earth Planet. Sci. Lett.*, *196*, 83–98, doi:10.1016/S0012-821X(01)00599-4.

Mitchell, T. D., and P. D. Jones (2005), An improved method of constructing a database of monthly climate observations and associated high-resolution grids, *Int. J. Climatol.*, *25*, 693–712, doi:10.1002/joc.1181.

Mokma, D. L., M. L. Jackson, and J. K. Syers (1973), Mineralogy and radioisotope retention properties of a chronosequence of soils developed in basalts of Victoria, Australia, *J. Soil Sci.*, *24*, 199–214.

Morison, J. I. L., and R. M. Gifford (1983), Stomatal sensitivity to carbon dioxide and humidity, *Plant Physiol.*, *71*, 789–796, doi:10.1104/pp.71.4.789.

New, M., M. Hulme, and P. D. Jones (2000), Representing twentieth century space-time climate variability, part 2: Development of 1901–96 monthly grids of terrestrial surface climate, *J. Clim.*, *13*, 2217–2238, doi:10.1175/1520-0442(2000)013<2217:RTCSTC>2.0.CO;2.

Oliva, P., J. Viers, and B. Dupré (2003), Chemical weathering in granitic environments, *Chem. Geol.*, *202*, 225–256, doi:10.1016/j.chemgeo.2002.08.001.

Paquet, H., G. Bocquier, and G. Millot (1966), Néoformation et dégradation des minéraux argileux dans certains solonetz

solodisés et vertisols du Tchad, *Bull. Serv. Carte Geol. Alsace Lorraine*, *19*, 295–322.

Peinemann, N., N. M. Amiotti, P. Zalba, and M. B. Villamil (2000), Effect of clay minerals and organic matter on the cation exchange capacity of silt fractions, *J. Plant Nutr. J. Sci.*, *163*, 47–52, doi:10.1002/(SICI)1522-2624(200002)163:1<47::AID-JPLN47>3.0.CO;2-A.

Pharande, A. L., and K. R. Sonar (1997), Clay mineralogy of some vertisol soil series of Maharashtra, *J. Indian Soc. Soil Sci.*, *45*, 373–377.

Pokrovsky, O. S., J. Schott, D. I. Kudryavtzev, and B. Dupré (2005), Basalt weathering in central Siberia under permafrost conditions, *Geochim. Cosmochim. Acta*, *69*, 5659–5680, doi:10.1016/j.gca.2005.07.018.

Probst, J. L., and Y. Tardy (1989), Global runoff fluctuations during the last 80 years in relation to world temperature change, *Am. J. Sci.*, *289*, 267–285.

Raymond, P. A., N.-H. Oh, R. E. Turner, and W. Broussard (2008), Anthropogenic enhanced fluxes of water and carbon from Mississippi River, *Nature*, *451*, 449–452, doi:10.1038/nature06505.

Reatto, A., A. Bruand, E. de Souza Martins, F. Muller, E. M. da Silva, O. A. de Carvalho Jr., M. Brossard, and G. Richard (2009), Development and origin of the microgranular structure in latosols of the Brazilian Central Plateau: Significance of texture, mineralogy, and biological activity, *Catena*, *76*, 122–134, doi:10.1016/j.catena.2008.10.003.

Roelandt, C., Y. Goddéris, M.-P. Bonnet, and F. Sondag (2010), Coupled modeling of biospheric and chemical weathering processes at the continental scale, *Global Biogeochem. Cycles*, *24*, GB2004, doi:10.1029/2008GB003420.

Rühlmann, J., M. Körschens, and J. Graefe (2006), A new approach to calculate the particle density of soils considering properties of the soil organic matter and the mineral matrix, *Geoderma*, *130*, 272–283, doi:10.1016/j.geoderma.2005.01.024.

Sanchez-Maranon, M., M. Soriano, M. Melgosa, G. Delgado, and R. Delgado (2004), Quantifying the effects of aggregation, particle size and components on the colour of Mediterranean soils, *Eur. J. Soil Sci.*, *55*, 551–565, doi:10.1111/j.1365-2389.2004.00624.x.

Schwanghart, W., and B. Schütt (2008), Holocene morphodynamics in the Ugii Nuur basin, Mongolia—Insights from a sediment profile and 1D electrical resistivity tomography, *Z. Geomorphol.*, *52*, 35–55, doi:10.1127/0372-8854/2008/0052S2-0035.

Shi, X. Z., D. S. Yu, E. D. Warner, X. Z. Pan, G. W. Petersen, Z. G. Gong, and D. C. Weindorf (2004), Soil database of 1:1,000,000 digital soil survey and reference system of the Chinese genetic soil classification system, *Soil Surv. Horizons*, *45*, 129–136.

Sitch, S., et al. (2003), Evaluation of ecosystem dynamics, plant geography and terrestrial carbon cycling in the LPJ dynamic global vegetation model, *Global Change Biol.*, *9*(2), 161–185, doi:10.1046/j.1365-2486.2003.00569.x.

Van Bavel, C. H. M. (1952), A soil aeration theory based on diffusion, *Soil Sci.*, *72*, 33–46.

Van de Geijn, S. C., and J. Goudriaan (1997), Changements du climat et production agricole, U.N. Food and Agric. Organ., Rome.

Walker, J. C. G., P. B. Hays, and J. F. Kasting (1981), A negative feedback mechanism for the long-term stabilization of Earth's surface temperature, *J. Geophys. Res.*, *86*, 9776–9782, doi:10.1029/JC086iC10p09776.

Watson, R. T., H. Rodhe, H. Oescheger, and U. Siegenthaler (1990), Greenhouse gases and aerosols, in *Climate Change: The IPCC Scientific Assessment*, edited by J. T. Houghton, G. J. Jenkins, and J. J. Ephraums, pp. 1–40, Cambridge Univ. Press, Cambridge, U. K.

Wiseman, C. L. S., and W. Püttmann (2006), Interactions between mineral phases in the preservation of soil organic matter, *Geoderma*, *134*, 109–118, doi:10.1016/j.geoderma.2005.09.001.

Woodward, F. I. (2002), Potential impacts of global elevated CO_2 concentrations on plants, *Plant Biol.*, *5*, 207–211.